




ARTICLE

Open Access

# Closed-eye intraocular pressure and eye movement monitoring via a stretchable bimodal contact lens

Xingyi Gan<sup>1</sup>, Guang Yao<sup>1,2,3</sup> , Cunbo Li<sup>4</sup>, Yufeng Mu<sup>4</sup>, Maowen Xie<sup>1</sup>, Chenzheng Zhou<sup>1</sup>, Peisi Li<sup>1</sup>, Qiwei Dong<sup>4</sup>, Ke Chen<sup>4</sup>, Kangning Zhao<sup>5</sup>, Min Gao<sup>1</sup>, Taisong Pan<sup>1</sup>, Fang Lu<sup>6</sup>, Dezhong Yao<sup>4</sup>, Peng Xu<sup>4</sup>  and Yuan Lin<sup>1,2,6</sup> 

## Abstract

Chronic ophthalmic diseases are multivariate, time-varying, and degenerative. Smart contact lenses have emerged as a scalable platform for noninvasive ocular signal detection and disease diagnosis. However, real-time monitoring and decoupling of multiple ocular parameters, particularly when the eyes are closed, remain challenging in clinical medicine. In this work, we propose a stretchable bimodal contact lens (BCL) amalgamating self-decoupled electromagnetic capacitive intraocular pressure (CIOP) and magnetic eye movement (MEM) monitoring components. The sandwich-integrated BCL can be intimately attached to the eyeball, enabling closed-eye, wireless, and precise signal acquisition without interference. During the eye open and closed, the serpentine-geometry CIOP unit was validated on a rabbit model, achieving supered resolution (1 mmHg) and sensitivity ( $\geq 0.22 \text{ MHz mmHg}^{-1}$ ) for reversible hypo- to hyper-IOP fluctuations. Ex vivo and in vivo MEM monitoring, based on composition-optimized magnetic interlayer film, demonstrated exceptional accuracy ( $\geq 97.25\%$ ) with eyes open and closed, surpassing existing methods. The collected CIOP and MEM data could be wirelessly aggregated and transmitted to portable devices via integrated acquisition modules within frame glasses for real-time eye healthcare. Emerging noninvasive and bimodal modalities reconcile the trade-off between minimal discomfort, eye status, and reliable measurement, spurring the widespread adoption of the integrated monitoring system for continuous ocular health monitoring.

**Keywords:** Bimodal contact lens; Self-decoupled; Intraocular pressure; Eye movement; Closed-eye monitoring

## Introduction

The eye plays a vital role in the eye-brain visual pathway, serving as a natural open window for retrieving information to construct vision and cognitive functions. According to a recent global survey by the Lancet Global Health Commission, chronic vision impairment plagued over 1.1 billion people worldwide in 2020, with 90% preventable and manageable<sup>1</sup>. Causes of chronic vision

impairment differ globally, with elevated intraocular pressure (IOP) and aberrant eye movement (EM) being indicative markers for conditions such as glaucoma<sup>2–4</sup> and attentional imbalance<sup>5,6</sup>, both flagged by time-varying and degenerative symptoms. Traditional devices, such as large-sized household tonometers<sup>7</sup> and eye trackers<sup>8</sup>, are prominently found in IOP and EM measurements. However, reliance on open-eye conditions limits their ability to capture continuous ocular signals and contributes to the significant medical, psychological, and economic burdens due to frequent hospital visits. Nocturnal intraocular pressure exhibits a significant circadian rhythm, typically peaking in the early morning hours before the end of sleep (3–4 mmHg higher than daytime levels), with a trough occurring at the end of the day. This phenomenon is closely associated with changes in body

Correspondence: Guang Yao ([gyao@uestc.edu.cn](mailto:gyao@uestc.edu.cn)) or Peng Xu ([xupeng@uestc.edu.cn](mailto:xupeng@uestc.edu.cn)) or Yuan Lin ([linyuan@uestc.edu.cn](mailto:linyuan@uestc.edu.cn))

<sup>1</sup>School of Materials and Energy, University of Electronic Science and Technology of China, 610054 Chengdu, Sichuan, China

<sup>2</sup>State Key Laboratory of Electronic Thin Films and Integrated Devices, University of Electronic Science and Technology of China, 610054 Chengdu, Sichuan, China

Full list of author information is available at the end of the article

© The Author(s) 2025



**Open Access** This article is licensed under a Creative Commons Attribution-NonCommercial-NoDerivatives 4.0 International License, which permits any non-commercial use, sharing, distribution and reproduction in any medium or format, as long as you give appropriate credit to the original author(s) and the source, provide a link to the Creative Commons licence, and indicate if you modified the licensed material. You do not have permission under this licence to share adapted material derived from this article or parts of it. The images or other third party material in this article are included in the article's Creative Commons licence, unless indicated otherwise in a credit line to the material. If material is not included in the article's Creative Commons licence and your intended use is not permitted by statutory regulation or exceeds the permitted use, you will need to obtain permission directly from the copyright holder. To view a copy of this licence, visit <http://creativecommons.org/licenses/by-nc-nd/4.0/>.

position (supine posture increases episcleral venous pressure by 3–6 mmHg) and fluctuations in glucocorticoid levels. Furthermore, frequent eye movements during sleep, such as those occurring during rapid eye movement (REM) sleep, can increase resistance to aqueous humor outflow. This is particularly concerning in patients with angle-closure glaucoma, where the risk of acute attacks is 3–5 times higher at night compared to during the day. Therefore, monitoring nocturnal intraocular pressure and eye movements is crucial<sup>9</sup>. This limitation is particularly problematic for monitoring hypo- to hyper-IOP fluctuations and abnormal EM, especially during closed-eye state and sleep, which are pivotal for tracking disease progression<sup>10,11</sup>. Therefore, achieving long-term dynamic and precise monitoring of these characteristic signals becomes imperative for early diagnosis and timely intervention to avoid treatment difficulty due to disease deterioration.

Smart contact lenses have emerged as a promising solution for continuous, noninvasive ocular signal monitoring instead of discrete measurements, offering a scalable platform for ophthalmic disease diagnosis<sup>12–22</sup>. Goldmann Applanation Tonometry (GAT) remains the gold intraocular pressure (IOP) measurement standard. However, GAT requires topical anesthesia and fluorescein instillation before measurement, and the fluorescein concentration can influence accuracy. Furthermore, GAT necessitates a slit lamp examination. Corneal thickness, stiffness, and tear film characteristics can also introduce measurement errors. Flexible electromagnetic contact lenses, for example, could realize continuous and non-invasive IOP monitoring by incorporating flexible electronic superiorities into wireless electromagnetic biosensing systems. Based on resistor-capacitor-inductor resonant circuits, these lenses correlate micro eyeball strain with electromagnetic parameters, translating dynamic IOP fluctuations into measurable signals<sup>23–30</sup>. This frequency shift is then wirelessly transmitted to an external readout coil via inductive coupling, enabling IOP determination while minimizing corneal and conjunctival damage and eliminating cable-related infection risks. Although this convenient modality facilitates IOP acquisition and quantification, challenges such as insufficient resolution, inadequate sensitivity, and restricted application scenarios hinder their widespread application. Corneal contact lenses are rapidly evolving for glaucoma management. Wireless theranostic contact lens (WTCL), utilizing cantilever capacitive sensing and other technologies, achieves ultra-sensitive intraocular pressure detection and on-demand drug release<sup>25</sup>. Similarly, the AuHNW-based WTCL system employs high-stability sensors and flexible drug delivery systems for precise drug release control<sup>27</sup>. Both exemplify a trend toward miniaturization and wireless functionality, facilitating a dynamic closed-loop approach to glaucoma management.

Scleral coil-based eye tracking is renowned for its high angular resolution and rapid response time and continues to be a benchmark technique<sup>31–33</sup>. However, the wired connection requires corneal anesthesia and is susceptible to slippage, significantly limiting user acceptability. For EM monitoring, previous research has primarily focused on specialized eye trackers such as pupil-center corneal reflection-based video oculography<sup>34,35</sup>, skin-patchable electrooculography electrodes<sup>36</sup>, and electromechanical conversion-driven strain/pressure sensors<sup>37</sup>. Electroretinogram (EOG)-based eye tracking utilizes skin electrodes to detect eye dipole potential signals, exploiting the cornea's and the retina's negative charges. While EOG primarily measures horizontal and vertical eye movements, it struggles to capture rotational and micro-movements accurately<sup>38</sup>. Recently, existing strategies for target EM monitoring with innovative trackers have revolutionarily rendered biorecognition systems portable, wireless, noninvasive, and precise features. However, reported research or contact lens-based systems were scarce to address personalized closed-eye EM monitoring, where eyelid blocking and blink artifacts inevitably compromise accuracy and reliability. Simultaneously, similar to other biomedical devices, future developments in smart contact lenses focus on multifunctionality, accuracy, and scalability. Integrating multiple sensing components to identify various stimuli presents a practical approach for multifunctional ocular signal detection. Recent research has explored electromagnetic induction frequency-coded smart contact lenses as promising wearable devices offering high precision, robustness, and blink-artifact immunity<sup>39</sup>. However, bulky structures, complex fabrication, severe signal interference, and intricate decoupling algorithms necessitate thorough investigation, assessment, and circumventing. Multimodal fusion flexible sensing technology, including pressure and temperature dual-modal tactile sensors and photoelectric tri-modal synchronous detection sensors, prioritizes high sensitivity and low crosstalk<sup>40,41</sup>. These technologies support applications such as electronic skin, health monitoring, and immersive interaction with intelligent robots, driving the widespread adoption of flexible sensing technology. Hence, sophisticated multifunctional sensing integration design, multimodal self-decoupled mechanisms establishment, and systematic multi-scenario accuracy evaluation will lay an essential foundation for developing a personalized, preventative, and closed-eye contact lens-based ophthalmic healthcare system.

This work proposes a stretchable self-decoupled BCL comprising electromagnetic capacitive IOP (CIOP) and neodymium-iron-boron (NdFeB)-MEM components. The design features an NdFeB/polydimethylsiloxane (PDMS) interlayer film that separates double-layered serpentine-geometry spiral copper (Cu) films. The optimized

structural geometry and NdFeB/PDMS composition rendered the BCL robust and sensitive, exhibiting prominent mechanical adaptability and high biorecognition resolution. This design minimizes cross-sensitive interference for multiple eyeball sizes, ensuring accurate data acquisition in both open- and closed-eye scenarios. Dynamic CIOP monitoring in a rabbit model showcased the BCL's superior resolution (1 mmHg) and high sensitivity for both open-eye ( $0.22 \text{ MHz mmHg}^{-1}$ ) and closed-eye ( $0.758 \text{ MHz mmHg}^{-1}$ ) conditions during reversible IOP fluctuations. EM monitoring accuracy was systematically evaluated using ex vivo and in vivo models, with results showing the open- and closed-eye MEM accuracy values were (99.375%, 97.5%) and (98.75%, 97.25%) for ex vivo and in vivo models, outperforming commercial and other noninvasive EM monitoring approaches. Furthermore, the collected information from the BCL could be wirelessly transmitted to portable devices through integrated acquisition modules embedded in frame glasses. This integrated system offers a non-invasive and comfortable solution for real-time eye health monitoring, providing accurate measurements and continuous tracking of eye status. This work established a BCL-based eye health monitoring strategy in a curve-integrated, self-decoupled, closed-eye paradigm. Multi-scenario applicability and functional scalability would empower the widespread adoption of this BCL system for personalized ophthalmic care. Its exceptional performance and tailored design open new possibilities for enhancing eye care and advancing research in the field.

## Results and discussion

### Design and characterization of the BCL

The design concept and working principle of the eye health monitoring system are illustrated in Fig. 1a. As shown in Fig. 1a(i), the system consisted of a noninvasive human-interface BCL for signal collection and a data acquisition unit embedded within a frame glasses lens, whose wireless configuration permits real-time ocular signal monitoring on open- or closed-eye status. The exploded view in Fig. 1a(ii) detailed the BCL's key components, essential materials, and multilayer structures. The sandwich-structured BCL comprises five layers: double-layer serpentine spiral Cu films driven by eyeball deformation for CIOP sensing, a NdFeB/PDMS composite film that functions as both a CIOP intermediate medium and the MEM sensing component, and two flexible PDMS encapsulation layers that conform to curved nondevelopable eyeball surface seamlessly and avoid potential erosion in the physiological environment. The detailed fabrication procedure for the BCL is outlined in Fig. S1, encompassing nanosecond laser patterning, NdFeB/PDMS composite preparation, transfer printing, integration, and packaging. Fig. 1a(iii) displays optical images of a BCL in various

states. The initial design mimics a cosmetic-colored contact lens to preserve pupil visibility and minimize interference with intrinsic vision. The BCL's dimensions in the initial state are  $\sim 14 \times 5 \times 0.2 \text{ mm}^3$  ( $\Phi \times H \times T$ ) (Fig. S2). Optimized serpentine spiral geometry and NdFeB/PDMS composition enhance mechanical robustness, lessen the overall modulus, and boost detection sensitivity, allowing the BCL to undergo substantial deformation, such as stretching and twisting. The experimental setup in Fig. 1a, iii (bottom) demonstrates the seamless attachment of the BCL to the eyeball. Bimodal sensing mechanisms render the BCL to discriminate EM and pressure stimuli for self-decoupled MEM and CIOP detection. An electromagnetic reader coil (connected to a mini vector network analyzer) and an eight-channel Tesla meter, integrated into frame glasses, could convert these collected signals into measurable CIOP and MEM data formats. Then, open- or closed-eye acquisition signals carrying dynamic hypo- to hyper-CIOP fluctuation and real-time MEM information are wirelessly aggregated and transmitted to portable devices for continuous eye health monitoring (Fig. 1a, iv).

The as-prepared BCL underwent comprehensive characterization and evaluation to assess its multilayer configuration, curvature adaptability, and in vivo biocompatibility. Firstly, we employed a three-dimensional (3D) microscope to examine the height information of the multilayer components. The side- and the top-view 3D scanning images revealed that all components' surface topography was flat and uniform (Figs. 1b and S3). A cross-sectional height profile was taken along a scanning line to gauge the multilayer thickness:  $30 \mu\text{m}$  for the top PDMS encapsulation layer,  $37 \mu\text{m}$  for the serpentine spiral Cu layer,  $61 \mu\text{m}$  for the NdFeB/PDMS interlayer, and  $30 \mu\text{m}$  for the bottom PDMS encapsulation layer (Fig. 1c), resulting in an overall cross-sectional thickness of  $\sim 195 \mu\text{m}$ . This thickness falls within the range of commercially available contact lenses for human wear. Secondly, curvature adaptability and mechanical robustness were assessed by a pressing system with a spherical plastic ball (diameter: 12 mm) in both finite element analysis (FEA) and experimental modalities, where the Cu coil turns number ( $C_n$ ) of the serpentine spiral coil was set as 5 (Fig. 1d). FEA and experimental results consistently indicated that the BCL exhibited curvature adaptability and mechanical robustness (Movie S1). The strain ( $<0.45\%$ ) consistently remained well below the failure strain ( $\sim 3\%$ ), even under stress distribution ranging from 0 to 10 mm in height (Fig. S4). Finally, biocompatibility was evaluated through animal studies using rabbits<sup>42</sup>. The rabbits wore the encapsulated BCL on their right eyes for a week without affecting their daily activity (Movie S2), followed by a histological examination of the rabbit corneas using hematoxylin-eosin (H&E) staining. The results

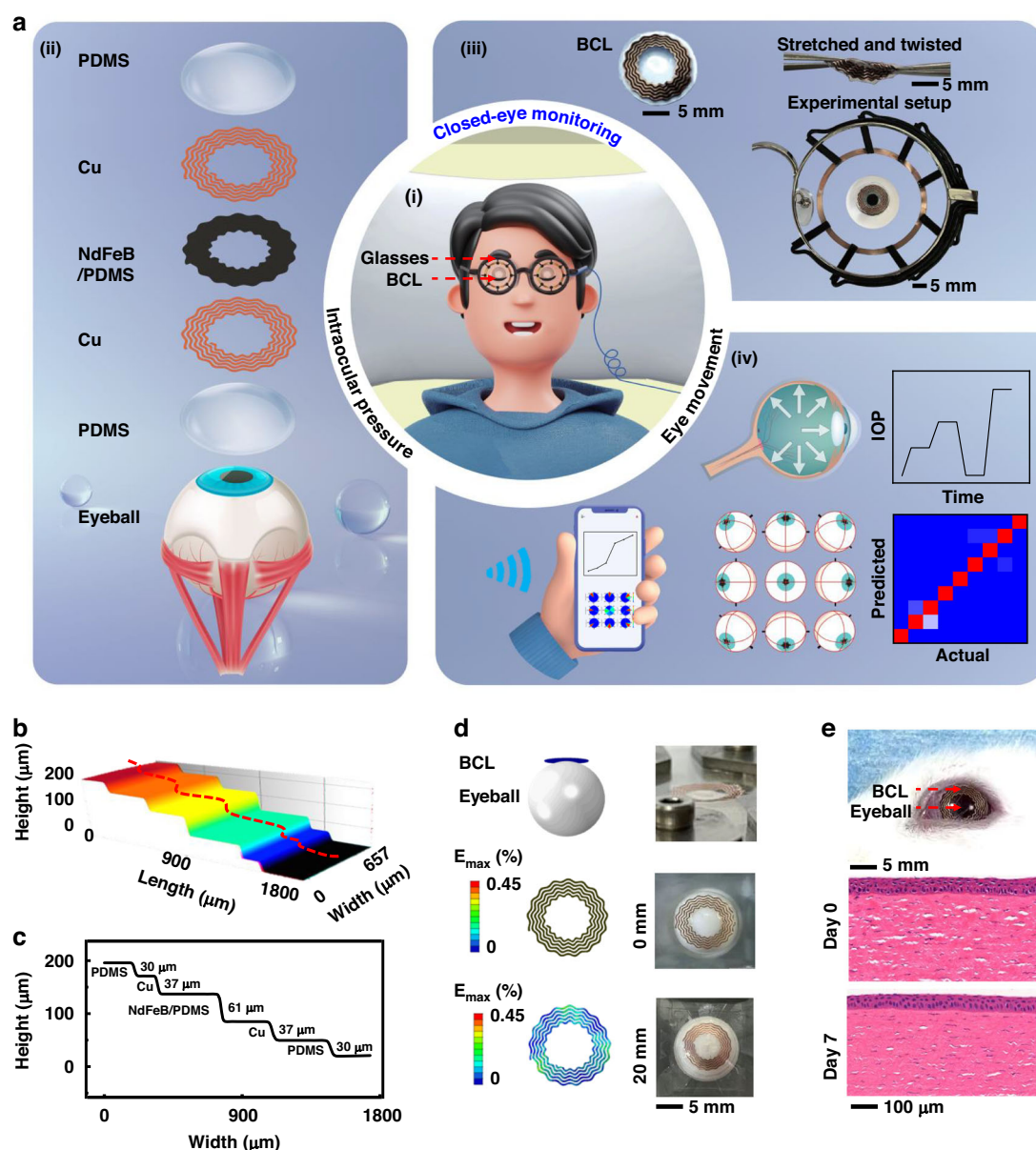
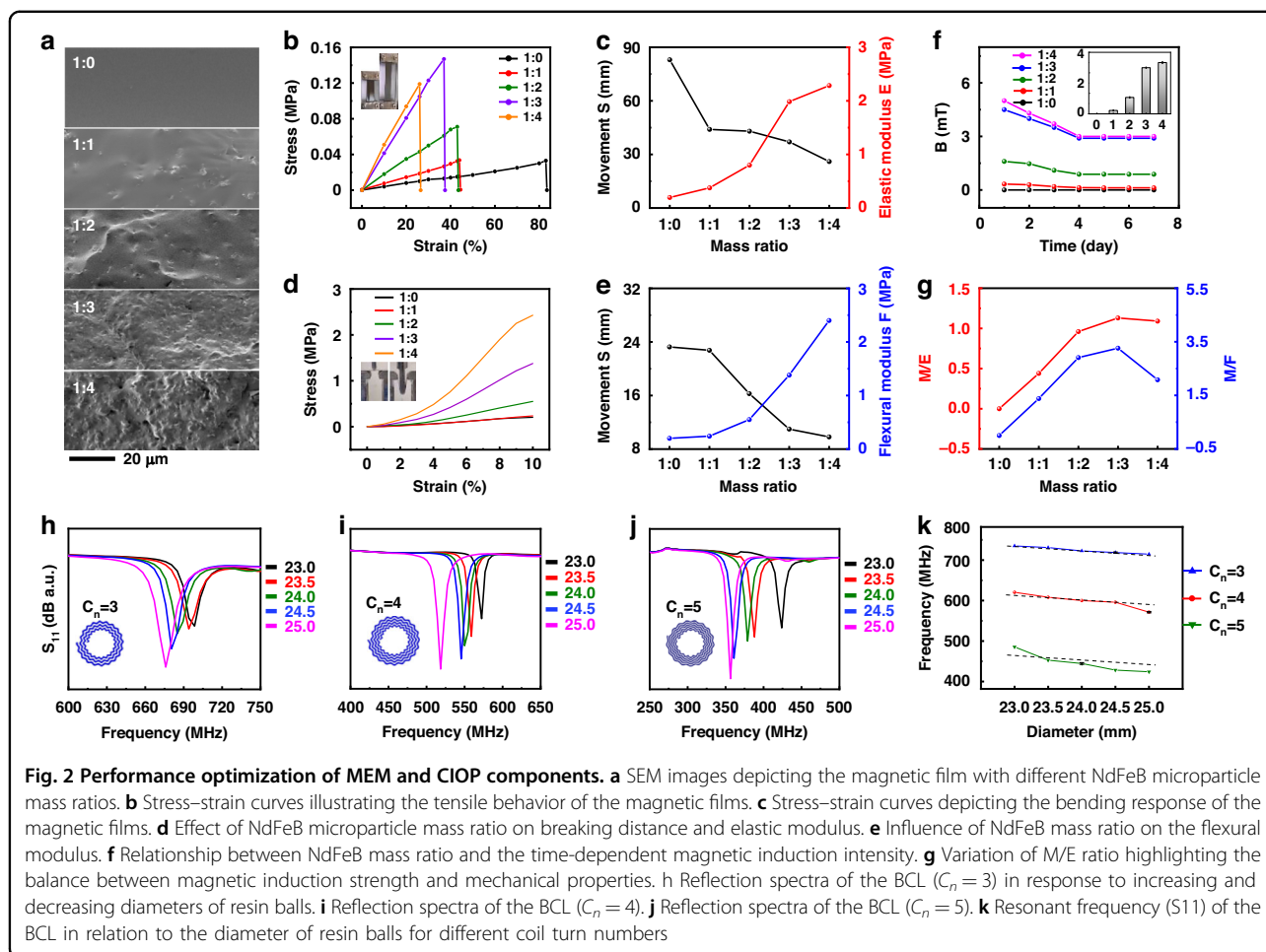


**Fig. 1 Design and characterization of the stretchable BCL.** **a** Design and working principle of the BCL. (i) Schematic diagram of BCL-based closed-eye capacitive intraocular pressure (CIOP) and magnetic eye movement (MEM) monitoring. (ii) Key components of the BCL. (iii) Optical images depicting the BCL in initial, stretched, and twisted states, and the experimental setup worn on an eyeball. (iv) Wireless transmission of CIOP and MEM signals to portable devices. **b** Three-dimensional image illustrating the thickness of various BCL components. **c** Height profile along the pink line in (b), displaying the height of multilayer components. **d** Finite element analysis (FEA) and experimental results of the BCL under a series of pressing heights, with corresponding experimental height results. **e** Biocompatibility Characterization of the BCL

revealed no signs of pathological inflammation, confirming that the encapsulated BCL is non-cytotoxic and biocompatible (Fig. 1e). As shown in Fig. S5, the cell viability using BCL extracts remained above 90% after 72 h of incubation, and there was no significant difference between the groups. These results indicate that long-term wear of the BCL is non-cytotoxic and presents a minimal risk of corneal inflammation. The corneal slit lamp results after

wearing for 48 h showed that BCL had no obvious damage to the eyes and had good biocompatibility (Fig. S6). The results from the open-field experiment indicate that the activity patterns of animals wearing the BCL along the site's perimeter exhibit a degree of regularity (Fig. S7). This suggests that the animals engage in exploratory and adaptive behaviors within the environment and that wearing the BCL does not impede their normal activities.





### Performance optimization of MEM and CIOP components

The sandwich-integrated MEM and CIOP components were optimized in terms of composite mass ratios and serpentine coil configuration, respectively. The magnetic interlayer was tailored by amalgamating NdFeB microparticles into PDMS to meet MEM mechanical properties and magnetic requirements. The mass ratio (PDMS: NdFeB) was designed to be 1:0, 1:1, 1:2, 1:3, and 1:4<sup>43</sup>. Scanning electron microscope (SEM) analysis of the NdFeB/PDMS cross-sectional surface revealed uniform morphologies, with the filling fraction of NdFeB microparticles increasing proportionally to the mass ratio (1:0 to 1:4), indicating the controllability of the mixing process (Fig. 2a). Subsequently, we investigated the mechanical properties of as-prepared NdFeB/PDMS films (~60  $\mu\text{m}$ ) under both stretching and bending modes. Stress-strain curves demonstrated in Fig. 2b, d revealed a monotonic increase in tensile and bending stresses with the scaled-up mass ratio. Notably, the film with a 1:3 mass ratio exhibited the highest tensile fracture stress (0.147 MPa), surpassing other groups (0.033 Mpa for 1:0, 0.034 Mpa for 1:1, 0.071 Mpa for 1:2, and 0.119 Mpa for 1:4) (Fig. 2c). In stretching mode, elastic modulus (E) and

fracture distance (FD) extrapolated from Fig. 2b were presented in Fig. 2c. Both E (0.39, 0.75, 1.6, 3.97, and 4.57 MPa) and FD (83, 44, 43, 37, and 26 mm) showed monotonic changes with increasing mass ratio, but in opposite trends. Similarly, in bending mode, flexural modulus (F) and movement distance (MD) were extracted from Fig. 2d (Fig. 2e). The (F, MD) were (0.2, 23.25), (0.24, 22.75), (0.55, 16.27), (1.38, 10.98), and (2.4, 9.81) for 1:0, 1:1, 1:2, 1:3, and 1:4 magnetic films, respectively. These results revealed that the composite flexibility weakened as the mass ratio increased. After magnetization under consistent conditions, the magnetic decay performance was quantitatively assessed over a 7-day period (Fig. 2f). The magnetic induction intensity rapidly attenuated from day 1 to day 4 and gradually decayed to a stable value at 15 mm. On day 7 (Inset in Fig. 2f), the magnetic induction intensity of 1:3 and 1:4 NdFeB/PDMS films were 2.8 and 3.1 mT (with no statistically significant difference), which was significantly higher than those of other films (0 mT for 1:0, 0.12 mT for 1:1, and 0.88 mT for 1:2). Additionally, we characterized the magnetization decay over distance and time (Fig. S8). Moreover, M/E and M/F were defined as critical parameters to balance

the magnetic induction strength and mechanical properties of the magnetic films (Fig. 2g)<sup>44</sup>. M/E and M/F values initially increased with the mass ratio, peaked at 1:3 (M/E = 1.13, M/F = 3.26), and then decreased. These values surpass M/E (0, 0.44, 0.96, and 1.09) and M/F (0, 1.38, 2.91, and 2.08) for other mass ratios (1:0, 1:1, 1:2, and 1:4). Given the comprehensive evaluation of the mechanical and magnetic properties, a mass ratio of 1:3 was selected for subsequent BCL integration. The proportion of neodymium iron boron (NdFeB) magnets within the magnetic interlayer critically influences the performance of BCL. Optimizing its mass ratio (e.g., 1:3) allows for an optimal balance between mechanical properties (elastic modulus, fracture distance) and magnetic properties (magnetic induction intensity, coercive force), thereby meeting the requirements for precise eye movement monitoring. Alternative materials, such as Fe<sub>3</sub>O<sub>4</sub>, cannot achieve the comprehensive benefits of NdFeB due to their low magnetic induction intensity and rapid demagnetization (Fig. S9). Similarly, high cost and poor temperature stability limit aluminum nickel cobalt and samarium cobalt. NdFeB achieves high remanence, high coercive force, and stable magnetic properties through inter-granular exchange coupling, grain boundary phase regulation, and magnetic powder particle size distribution optimization. Currently, no other material offers a comparable combination of properties for high-precision flexible magnetic devices.

We further investigated the double-layered spiral coil design within the CIOP component to achieve optimal sensing performance. The insets of Fig. 2h–j illustrate various design and parameter calibrations for the serpentine spiral Cu coil. The coordinates ( $X_1$ ,  $Y_1$ ) on the outer boundary and ( $X_2$ ,  $Y_2$ ) on the inner boundary were determined by the following formulae 1–4:

$$X_1 = a_1 + 0.1 \times (t + 2 \times \sin(t * 20) \times \cos(t)) \quad (1)$$

$$Y_1 = a_1 + 0.1 \times (t + 2 \times \sin(t * 20) \times \sin(t)) \quad (2)$$

$$X_2 = a_2 + 0.1 \times (t + 2 \times \sin(t * 20) \times \cos(t)) \quad (3)$$

$$Y_2 = a_2 + 0.1 \times (t + 2 \times \sin(t * 20) \times \sin(t)) \quad (4)$$

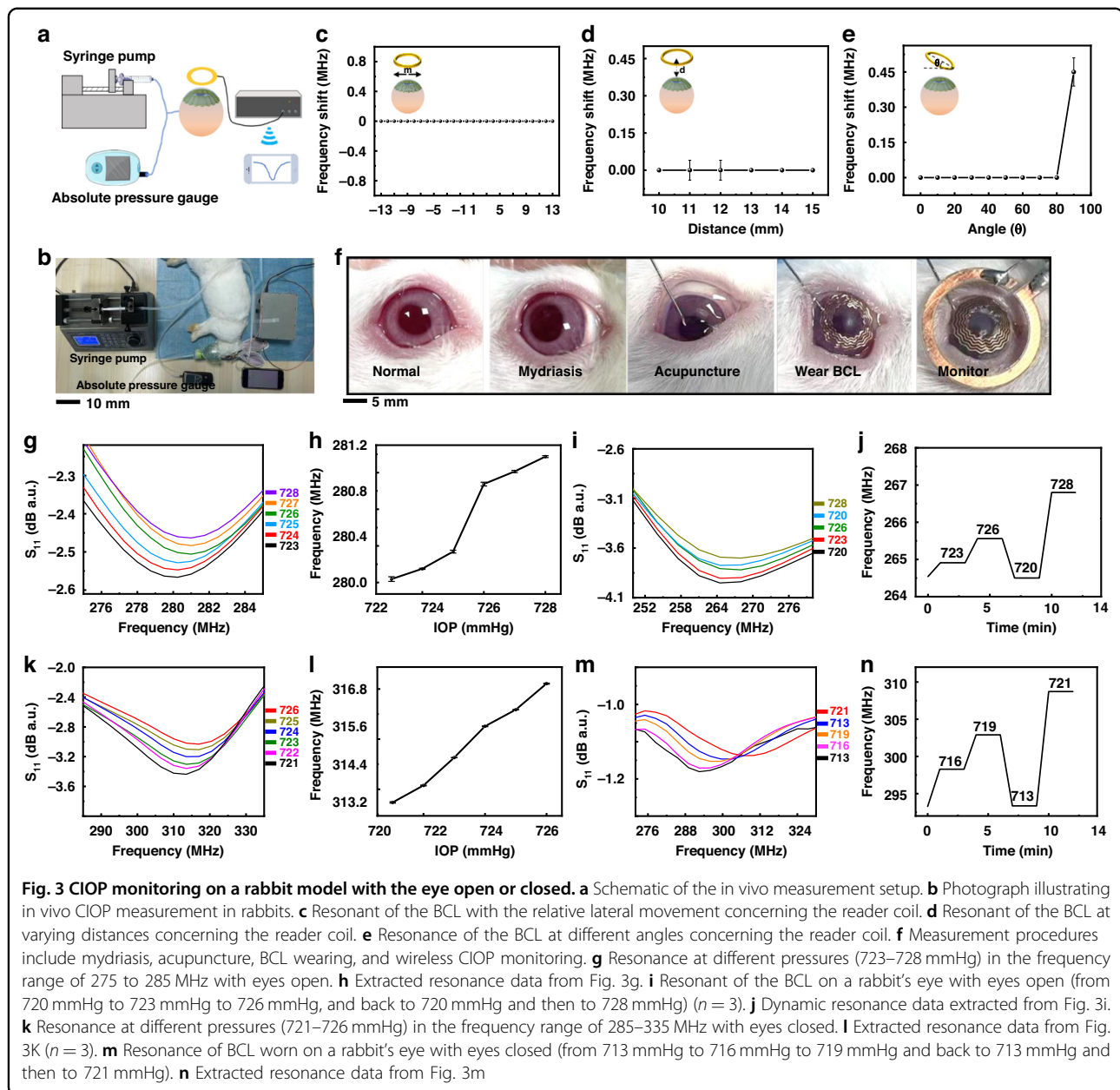
where  $a$  represents the distance from the starting point of the spiral to the origin, and  $t$  is the radian. The coil wire width is determined by the difference between  $a_1$  and  $a_2$ . The number of coil turns is controlled by  $t$  (Fig. S10). We designed  $C_n$  (Cu coil turns number) as 3, 4, and 5, with equal line width and gap, and estimated their mechanical properties. FEA results under biaxial tensile strain (0–20%) demonstrated that the strain (<0.45%) was consistently smaller than the failure strain (~3%)<sup>45</sup> that appeared on the spiral coil. The defined stretchability was 12%, 16%, and 20% when the  $C_n$  was 3, 4, and 5, respectively (Fig. S11). These

results indicated that the fractal serpentine geometry could promote mechanical robustness, with the spiral coil ( $C_n = 5$ ) showing the best stretchability.

In vitro, CIOP sensitivity and curvature adaptability were characterized using spherical plastic balls that mimicked human eyeball dilation (diameter ranging from 23 mm to 25 mm in 0.5 mm intervals)<sup>29</sup>. The resonant was wirelessly transmitted by a reader coil (height = 10 mm) connected to a standard vector network analyzer (VNA, Rohde & Schwarz, ZNB 20). As shown in Fig. 2h–j, resonant peaks were clearly distinguishable and shifted progressively as the ball diameter increased from 23 mm to 25 mm. The distribution intervals of resonant points were (698.5 MHz, 676.0 MHz), (572.5 MHz, 518.5 MHz), and (424.0 MHz, 356.5 MHz) for  $C_n = 3, 4$ , and 5, respectively. The corresponding change rates were 3.22%, 9.43%, and 15.92%. The absolute resonant frequencies for various ball dimensions extracted from Fig. 2h–j were demonstrated in Fig. 2k. For  $C_n = 3, 4$ , and 5, the corresponding responsivities were 11.25 MHz mm<sup>-1</sup>, 27 MHz mm<sup>-1</sup>, and 33.75 MHz mm<sup>-1</sup>, indicating that spiral coil with  $C_n = 5$  exhibited the best detection sensitivity for dynamic curvature changes. Furthermore, the CIOP component seamlessly and repeatedly attached to various balls without any structural damage, demonstrating outstanding curvature adaptability and mechanical robustness. Compared to other geometric parameters ( $C_n = 3$  and 4), the spiral coil ( $C_n = 5$ ) demonstrated optimized performance across sensitivity, stretchability, curvature adaptability, and mechanical robustness. Consequently, the spiral coil with  $C_n = 5$  was chosen for further CIOP integration and animal studies.

#### CIOP monitoring on a rabbit model of the BCL

After optimizing the magnetic performance of the MEM component and sensitivity of the CIOP component, BCLs were integrated following the BCL fabrication procedure described in Fig. S1 based on a double-layered spiral coil ( $C_n = 5$ ) and NdFeB/PDMS (3:1) interlayer film. A BCL-based CIOP verification system was set up (Fig. 3a), comprising a needle for eye stuck, a syringe pump for saline injection, and a pressure gauge for IOP calibration, all connected via tee-connected hoses. Considering the system's feasibility, a portable and wireless communication-supported VNA was designed for CIOP acquisition<sup>46</sup> (Fig. 3b). To assess the impact of lateral displacement on the resonant frequency, we varied the lateral movement ( $m$ ) from -13 mm to 13 mm in 1 mm increments (Fig. 3c). The results showed no statistically significant frequency shift within this range ( $-13 \text{ mm} \leq m \leq 13 \text{ mm}$ ) and vertical distance vertical distance between BCL and reader coil (set to be from 10 mm to 15 mm), indicating that the system is robust to user misalignment or displacement without significant performance degradation (Fig. S12). Additionally, the  $d$  (vertical distance between BCL and reader coil) was



set to be from 10 mm to 15 mm (in 1 mm intervals). The  $\theta$  (horizontal angle between BCL and reader coil) was adjusted from  $0^\circ$  to  $90^\circ$  (in  $10^\circ$  intervals) to assess their impact on resonant frequency (Fig. 3d, e). No statistically significant frequency shift was observed when  $\theta \leq 80^\circ$  and  $d \leq 15$  mm, indicating that this system could tolerate user misalignment or displacement without a noticeable degradation (Fig. S13).

The BCL-based CIOP system was verified in vivo on a rabbit model, spanning hypo- to hyper-IOP levels. The experimental protocol sequentially involved mydriasis, acupuncture, BCL wearing, and wireless CIOP monitoring<sup>45,47</sup> (Fig. 3f). It is worth noting that saline solution was injected

using a microinjection pump, allowing precise control over the injected volume and more accurately simulating fluctuations in IOP<sup>48,49</sup>. In Fig. 3g, the CIOP signal from the open eye exhibited a monotonic shift as IOP increased (723–728 mmHg), with the BCL's initial resonant point at 280.18 MHz. Remarkably, the shifting trend reversed with the increase in the ball radius, attributed to the reduction in eyeball curvature as IOP rose<sup>45</sup>. The resonant frequencies extracted from Fig. 3g exhibited a linear response, with a sensitivity of  $0.22 \text{ MHz mmHg}^{-1}$  for IOP measurement (Fig. 3h). The system was further evaluated under reversible hypo- to hyper-IOP levels (720–728 mmHg). The CIOP value underwent dynamic reversible changes with the IOP

controlled by the microinjection pump (Fig. 3i). Moreover, the CIOP signal maintained a long-term value corresponding to the IOP (Fig. 3j). The CIOP was also monitored with the rabbit's eyes closed. The initial resonant point of the BCL was 313.18 MHz, and CIOP exhibited a monotonic change from 721 to 726 mmHg during the IOP increase (Fig. 3k). The eyelid induced a slight deviation in the initial frequency point. Similarly, The extracted resonant frequencies from Fig. 3k displayed a linear response, with a sensitivity of  $0.758 \text{ MHz mmHg}^{-1}$  for IOP measurement (Fig. 3l). When the eyes were closed, the snug fit between the BCL and the eyeball may result in higher sensitivity during monitoring. (Fig. 3m). Likewise, the CIOP signal under eyes-closed conditions consistently maintained long-term values corresponding to IOP levels (Fig. 3n). The relative permittivity of human tissue varies with frequency<sup>50</sup>. In the low-frequency range, the relative permittivity is higher, enhancing electric field coupling and increasing the coils' mutual inductance. We conducted simulation experiments using animal eyeballs and artificial eye models (Fig. S14a). Simulation results show a frequency shift of approximately 100 MHz upon introducing biological tissue (Fig. S14b). This finding was corroborated by experimental results demonstrating a similar frequency shift under the influence of living animal eyes (Fig. S14c). Therefore, when accounting for the influence of biological tissue, the calibration curve obtained from the rabbit model aligns with the *in vitro* calibration curve. This innovative BCL demonstrated remarkable accuracy in detecting IOP, regardless of whether the eyes are open or closed. In comparison to other reported wearable devices, it boasted superior resolution and sensitivity (Table S1), making it an ideal tool for the timely detection of elevated IOP and the diagnosis of associated diseases.

#### Ex vivo and in vivo MEM monitoring of the BCL

To enable dynamic EM decoding for eye-disorder diagnosis, we established a real-time MEM monitoring and tracking platform utilizing a wearable BCL and an 8-channel Tesla meter integrated into a frame glasses lens (Movie S3). The gaze point and EM trajectory are determined by the distribution of magnetic induction intensity. This innovative system leverages the spatial relationship between the pre-magnetized BCL and frame glasses, distinguishing it from previously reported wearable trackers. As illustrated in Fig. 4a, gaze points are configured in a  $3 \times 3$  grid on a screen, numbered from 1 to 9. When the gaze point transitions between grids, the BCL-based MEM system records the EM trajectory as a magnetic signal. This signal is then decoded into movement directions using deep learning and displayed as a motion path on the grid. The working framework comprises a grid screen, a real-time eye-tracking camera, and magnetic output from the Tesla meter array. Vertical and horizontal eye movements are deconstructed into 8 directions: 4 linear (up,

down, right, left) and 4 diagonal (upper-right, upper-left, lower-right, lower-left). The associated EM angles are ( $0^\circ$ ,  $180^\circ$ ,  $90^\circ$ ,  $270^\circ$ ) for linear movements and ( $45^\circ$ ,  $315^\circ$ ,  $135^\circ$ ,  $225^\circ$ ) for diagonal ones. Each detection direction corresponds to a unique random trajectory.

To fine-tune the *ex vivo* MEM system, we created an artificial human head model with freely rotating eyeballs. The artificial eyeball wore a BCL, and the frame glasses were positioned approximately 10 mm away. Magnetic induction data, captured by the 8-channel Tesla meter (Channel I-VIII), were investigated during open-eye periocular movements, with no obstruction between the BCL and frame glasses (Fig. 4b). At gaze point 5, magnetic signals from all 8 channels exhibited similar values ( $\sim 0.08 \text{ mT}$ ), signifying the eye was looking straight ahead. When the gaze shifted upward to point 2, magnetic signals from Channels I-IV increased, while Channels V-VIII decreased. Notably, magnetic signals returned to their baseline values when the gaze returned to the initial position (Fig. 4c). Visualized MEM heatmaps in Fig. 4d were generated based on channel magnetic signals extracted from Fig. 4c, revealing that EM could be accurately decoded with deep learning via an EM neural network (Fig. S15). Following 10 training rounds, the system achieved recognition accuracy of 99.375% with low training loss, indicating high predictive performance for EM decoding (Fig. 4e). For closed-eye movement scenarios, a 2-mm thick piece of mammalian skin was placed over the BCL to mimic the eyelid. With the gaze fixed on point 5, the average magnetic signal across all channels was  $\sim 0.04 \text{ mT}$ , reflecting a 50% attenuation compared to open-eye measurements (Fig. 4f). Despite this attenuation, MEM could be sensitively monitored and recorded during random EM patterns (Fig. 4g). Visualized MEM heatmaps extracted from Fig. 4h indicated the system's reliability and stability during closed-eye gaze movements, achieving a recognition accuracy of 97.5% (Fig. 4i). After validating the *ex vivo* MEM system, we assessed its feasibility *in vivo* by recruiting volunteers. Leveraging the flexible BCL and the portable acquisition system, volunteers comfortably wore the BCL and frame glasses. At gaze point 5, the 8-channel magnetic values were approximately  $0.07 \text{ mT}$  for open-eye and  $\sim 0.03 \text{ mT}$  for closed-eye conditions, indicating consistency between *ex vivo* and *in vivo* scenarios. The BCL-based system adeptly monitored random EM patterns, accurately reflecting the spatial magnetic distribution and achieving effective EM monitoring (Fig. 4j, k). After five rounds of random EM patterns, the open- and closed-eye MEM accuracy reached 97.5% and 97.25%, respectively, showcasing robust performance for the *in vivo* model (Fig. 4l, m). Compared to other wearable devices reported in the literature, the BCL system stands out due to its compact design, portability, and cost-effectiveness (Table S2), making it a promising candidate for future clinical applications. We utilized a human head model to demonstrate the simultaneous detection of intraocular pressure and



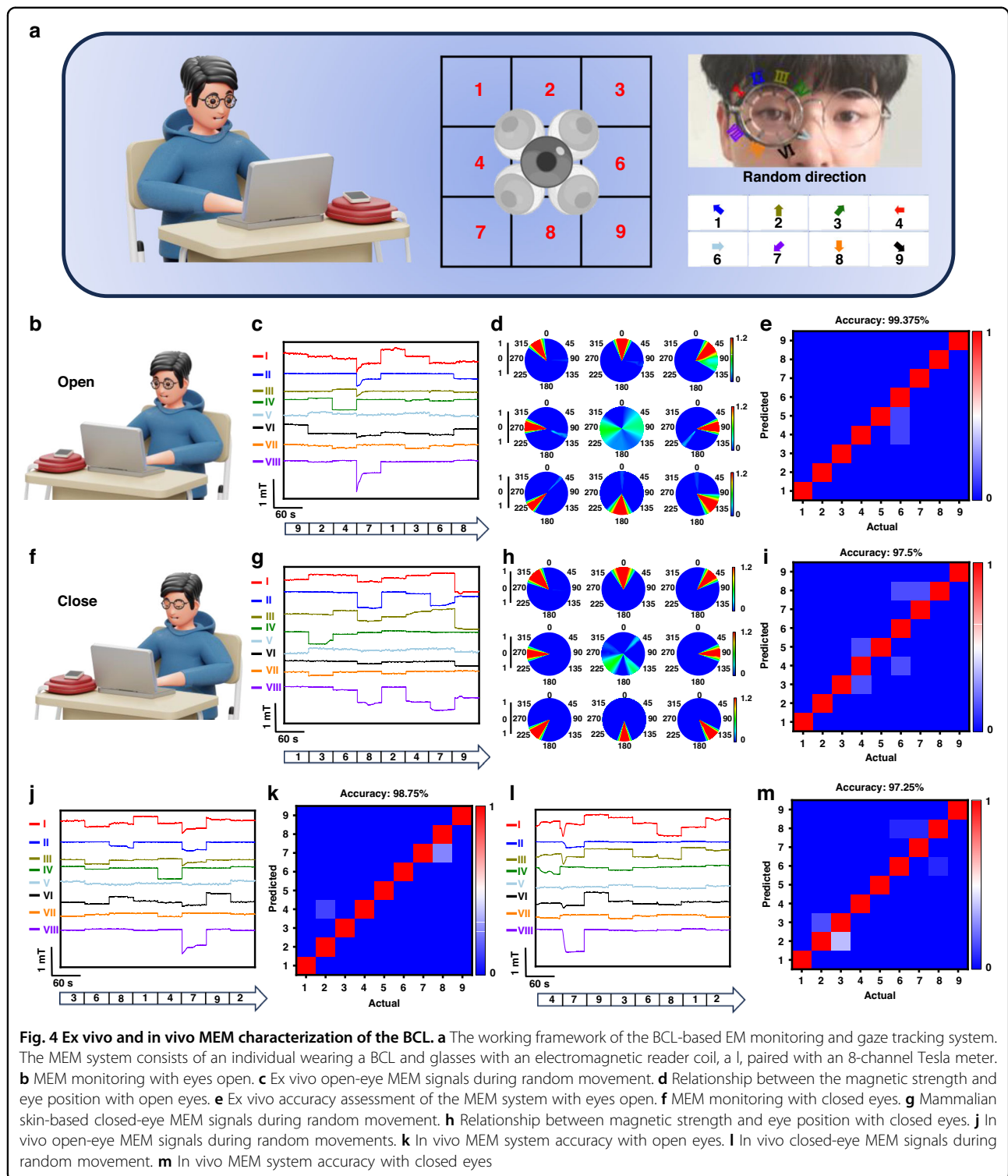


**Fig. 4** Ex vivo and in vivo MEM characterization of the BCL. **a** The working framework of the BCL-based EM monitoring and gaze tracking system. The MEM system consists of an individual wearing a BCL and glasses with an electromagnetic reader coil, a I, paired with an 8-channel Tesla meter. **b** MEM monitoring with eyes open. **c** Ex vivo open-eye MEM signals during random movement. **d** Relationship between the magnetic strength and eye position with open eyes. **e** Ex vivo accuracy assessment of the MEM system with eyes open. **f** MEM monitoring with closed eyes. **g** Mammalian skin-based closed-eye MEM signals during random movement. **h** Relationship between magnetic strength and eye position with closed eyes. **j** In vivo open-eye MEM signals during random movements. **k** In vivo MEM system accuracy with open eyes. **l** In vivo closed-eye MEM signals during random movement. **m** In vivo MEM system accuracy with closed eyes

eye movement. Intraocular pressure variations were simulated by employing eyeball models with varying radii (23.5 mm, 24 mm, and 24.5 mm). The resonant frequency shifted by the radius changes. We also performed eye

movement detection, successfully recording the induced eye movements. The results demonstrate the system's capability to simultaneously detect intraocular pressure and eye movement (Movie S4).

## Conclusion

This study presents an innovative, portable acquisition system that marries a flexible BCL with a robust data acquisition unit. Crafted from stretchable design and fabrication, the contact lens integrates a CIOP monitoring unit and an NdFeB-MEM monitoring unit, capable of withstanding up to 20% tensile strain. This unique design allows the lens to conform closely to the curvature of the eyeball, facilitating wireless and precise closed-eye ocular signal acquisition. The CIOP monitoring was validated on a rabbit model, demonstrating exceptional resolution (1 mmHg) and the ability to detect IOP (open eye:  $0.22 \text{ MHz mmHg}^{-1}$ , closed eye:  $0.758 \text{ MHz mmHg}^{-1}$ ) with high sensitivity. The system also showed dynamic monitoring capabilities during reversible hypotony-to-hypertensive fluctuations. In both ex vivo and in vivo MEM models involving healthy volunteers, the MEM monitoring unit exhibited remarkable accuracy in both open-eye (99.375%, 97.5%) and closed-eye (98.75%, 97.25%) conditions, surpassing alternative monitoring approaches. The acquired CIOP and MEM data can be wirelessly transmitted to portable devices via acquisition modules integrated into frame glasses. This integrated system offers a non-invasive, comfortable solution for real-time eye health monitoring, ensuring precise measurements and continuous tracking of eye status. With its potential for broad application across various scenarios, the wireless BCL-based system shows promise for advancing disease diagnosis, treatment, and daily ocular health management. Its exceptional performance and tailored design open new possibilities for enhancing eye care and advancing research in the field.

## Experimental section

### Ethics approval

All animal and human participant experiments were conducted in accordance with a standard protocol (1061420210617007) approved by the Ethics Committee of the Animal Experiment Center at the University of Electronic Science and Technology of China.

### Preparation of magnetic film

The preparation process is detailed in Fig. S1a, Supporting Information. The magnetic composite material is composed of isotropic NdFeB particles with a particle size of  $20 \mu\text{m}$ . (Magnequench Co., Ltd.) and PDMS (Sylgard 184, Dow Corning, Inc.) in a 10:1 mass ratio. The mixture was then spin-coated onto a glass substrate for 40 s and cured at  $60^\circ\text{C}$  for 60 min. After curing, the magnetic film was peeled off from the glass. The membranes were magnetized uniaxially using a magnetizer (ME-1225, Magele Technology Co., Ltd.) at 1200 V for three cycles to achieve saturation.

### Serpentine-geometry spiral design

Inspired by Archimedes' spiral, the serpentine geometry spiral design features a variable number of turns, which

can be adjusted by modifying the initial and end arcs. This design enables a reduction in arc length as the number of turns increases, offering design flexibility. We fixed  $C_n$  (number of copper coil turns) for this experiment at 3, 4, and 5. To enhance IOP monitoring sensitivity (Table S1), we controlled IOP with a syringe pump, enabling precise regulation of intraocular pressure changes.

### Fabrication of BCL

The detailed preparation process is illustrated in Fig. S1b. First, Cu film was adhered to the water-soluble tape (Shenzhen Yueda New Material Co., Ltd). The film was patterned to serpentine spiral coil structures by femtosecond laser cutting technology (laser power  $\sim 2.0 \text{ W}$ , Design Comes True Technology Co., Ltd, DirectLaser PC6). Subsequently, PDMS liquid A and liquid B were mixed in a 1:10 ratio and blended to form a homogeneous mixture. 1.5 mL of this mixture was dispensed onto a slide and spin-coated at 1000 rpm for 20 s. After heating at  $60^\circ\text{C}$  for 20 min, the upper layer of the serpentine spiral coil was transferred onto the PDMS material. This process was repeated to transfer the lower layer. The magnetic film was then shaped using a UV nanosecond laser cutter. The resulting serpentine spiral coil was sandwiched with the magnetic film, placed into a corneal contact lens mold, and filled with the PDMS mixture. The structure was then cured at  $60^\circ\text{C}$  for 10 h and removed from the mold.

### FEA mechanical characterization

The FEA mechanical properties of the BCL with different  $C_n$  (3, 4, and 5) and normal coils were evaluated by the ABAQUS 6.14 software. For Cu and PDMS, Young's modulus and Poisson's ratio were set to (119 GPa, 0.34) and (2 MPa, 0.49), respectively. Strain distribution for BCL ( $C_n = 5$ ) was analyzed under various pressing heights (0–10 mm) using a spherical ball with a 24 mm diameter. The strain ( $\leq 0.45\%$ ) subjected by the BCL was smaller than the failure strain ( $\sim 3\%$ ) even when the BCL was pressed up to 10 mm (Figs. 1d and S4d). Similarly, the strain ( $\leq 0.45\%$ ) of BCL ( $C_n = 5$ ) was also below the failure strain ( $\sim 3\%$ ) when the BCL was biaxially stretched to 20% (Fig. S11).

### In vivo biocompatibility validation of the BCL

Biocompatibility v was validated in vivo using a rabbit model. Optical images revealed that the BCL was well-associated without causing any corneal tissue injury throughout the entire 2-week observation period. Furthermore, H&E staining demonstrated the absence of any significant changes or inflammatory cell infiltration.

### Deep learning through the EM neural network

The MEM system employs innovative technology to capture and analyze changes in the annular magnetic field signals induced by EM, facilitating a novel human-

computer interface. It comprises several components, including BCLs, acquisition modules, signal analysis, and output control. The system works by detecting magnetic field changes corresponding to EM, with the signal acquisition unit transmitting data to a computer system. The data undergoes preprocessing to filter noise, followed by feature extraction to capture eye movement information. The extracted features are then input into a multi-class support vector machine to construct a hyperplane, allowing accurate classification of eye movements.

### Rabbit eyeball experiments

Following the anesthesia and pupil dilation, tee-connected hoses were connected to an absolute manometer (511; Testo, Inc.), a syringe pump, and a scalp needle. The scalp needle was inserted into the rabbit's posterior chamber. Fluctuations in IOP caused changes in corneal curvature, which deformed the BCL. The dynamic IOP led to changes in the coupling frequency of the receiving coil, enabling continuous monitoring of IOP variations. Wireless resonance frequency changes were measured using a network analyzer (Rohde & Schwarz, ZNB 20).

### Cytotoxicity assay

The viability of human corneal cells (HCE-T) was measured. The lenses were immersed in cell culture medium for 24 h to prepare BCL extracts. The cells were cultured with the extracts for different incubation times (12 h, 24 h, 48 h, and 72 h), and then CCK-8 reagent was added and the absorbance was measured to record cell viability.

### Human research participants

Two volunteers (Participant I, 23 years old, and Participant II, 22 years old) participated in the eye-tracking experiment. Prior to the experiment, both participants reviewed the research materials and received detailed explanations with satisfactory answers to their questions. They fully understood the medical research materials, including the associated risks and benefits. Participation was voluntary, and both participants were informed of their right to withdraw at any time. All human participant experiments followed a standard protocol (1061420210617007) approved by the Ethics Committee of the Animal Experiment Center at the University of Electronic Science and Technology of China.

### Execution of the Eye tracking system

As depicted in Figs. 1a and 4b, the Tesla meter is integrated into glasses, with its geometric center aligned to the wearer's pupil. The 8 channels of the Tesla meter are connected to a multi-channel data acquisition device. Before wearing the BCL, the subject applies eye drops to clean the eyes. After donning the BCL and glasses, calibration begins via a calibration interface. The subject then

follows instructions to perform a series of eye movements (five trials with randomly generated movement directions). The magnetic signals captured during these movements are processed and converted into eye movement signals.

### Acknowledgements

This work was supported by the National Natural Science Foundation of China under grant numbers 62422104, U21A20460, 62371115, 52021001; Science and Technology Major Project of Tibetan Autonomous Region of China under grant no. XZ202201ZD0001G; Science and Technology Department of Sichuan Province under grant no. 2024NSFSC0234; and the Medico-Engineering Cooperation Funds, Fundamental Research Funds for the Central Universities, UESTC under grant nos. ZYGX2020ZB041, ZYGX2021YGLH002.

### Author details

<sup>1</sup>School of Materials and Energy, University of Electronic Science and Technology of China, 610054 Chengdu, Sichuan, China. <sup>2</sup>State Key Laboratory of Electronic Thin Films and Integrated Devices, University of Electronic Science and Technology of China, 610054 Chengdu, Sichuan, China. <sup>3</sup>Shenzhen Institute for Advanced Study, University of Electronic Science and Technology of China, Shenzhen, 518110 Guangdong, China. <sup>4</sup>Clinical Hospital of Chengdu Brain Science Institute, MOE Key Lab for Neuroinformation, University of Electronic Science and Technology of China, 611731 Chengdu, Sichuan, China. <sup>5</sup>State Key Laboratory of Advanced Technology for Materials Synthesis and Processing, International School of Materials Science and Engineering, Wuhan University of Technology, 430070 Wuhan, Hubei, China. <sup>6</sup>Medico-Engineering Cooperation on Applied Medicine Research Center, Department of Ophthalmology, Sichuan Academy of Medical Sciences and Sichuan Provincial People's Hospital, University of Electronic Science and Technology of China, 610054 Chengdu, Sichuan, China

### Author contributions

G.Y. conceived the concept; G.Y., Y.L., and P.X. discussed, finalized the project plan, and supervised the project; Y.L., D.Y., K.C. and P.X. provided lab assistance; G.Y. and X.G. designed the device; X.G., C.L., Y.M., and M.X. performed the experiments and generated data in all figures; Q.D., Q.W., C.Z., P.L. and N.Z. participated in part of the experiments and optimized the experimental plan; G.Y., Y.L., X.G. T.P., F.L., and M.G. analyzed the data; G.Y., Y.L., and X.G. wrote the manuscript. All authors reviewed and commented on the manuscript. All authors read and approved the final manuscript.

### Data availability

The data that support the findings of this study are available from the corresponding author upon reasonable request.

### Conflict of interest

The authors declare no competing interests.

**Supplementary information** The online version contains supplementary material available at <https://doi.org/10.1038/s41378-025-00946-y>.

Received: 26 December 2024 Revised: 17 March 2025 Accepted: 8 April 2025

Published online: 12 May 2025

### References

- Burton, M. J. et al. The Lancet Global Health Commission on Global Eye Health: vision beyond 2020. *Lancet Glob. Health* **9**, e489–e551 (2021).
- Jonas, J. B. et al. Glaucoma. *Lancet* **390**, 2183–2193 (2017).
- Quigley, H. A. Glaucoma. *Lancet* **377**, 1367–1377 (2011).
- Weinreb, R. N., Aung, T. & Medeiros, F. A. The pathophysiology and treatment of glaucoma: a review. *JAMA* **311**, 1901–1911 (2014).
- Armstrong, T. & Olatunji, B. O. Eye tracking of attention in the affective disorders: a meta-analytic review and synthesis. *Clin. Psychol. Rev.* **32**, 704–723 (2012).

6. Fang, L., Sanchez-Lopez, A. & Koster, E. H. W. Attentional scope, rumination, and processing of emotional information: An eye-tracking study. *Emotion* **19**, 1259–1267 (2019).
7. Mostafa, I., Bianchi, E., Brown, L. & Tatham, A. J. What is the best way to measure intraocular pressure (IOP) in a virtual clinic? *Eye (Lond.)* **35**, 448–454 (2021).
8. Qian, K. et al. An eye tracking based virtual reality system for use inside magnetic resonance imaging systems. *Sci. Rep.* **11**, 16301 (2021).
9. Flatau, A. et al. Measured Changes in Limbal Strain During Simulated Sleep in Face Down Position Using an Instrumented Contact Lens in Healthy Adults and Adults With Glaucoma. *JAMA Ophthalmol.* **134**, 375–382 (2016).
10. Aptel, F., Weinreb, R. N., Chiquet, C. & Mansouri, K. 24-h monitoring devices and nyctohemeral rhythms of intraocular pressure. *Prog. Retin Eye Res.* **55**, 108–148 (2016).
11. Pronin, S., Brown, L., Megaw, R. & Tatham, A. J. Measurement of intraocular pressure by patients with glaucoma. *JAMA Ophthalmol.* **135**, 1030–1036 (2017).
12. Farandos, N. M., Yetisen, A. K., Monteiro, M. J., Lowe, C. R. & Yun, S. H. Contact lens sensors in ocular diagnostics. *Adv. Health. Mater.* **4**, 792–810 (2015).
13. Hughes, E., Spy, P. & Diamond, J. 24-h monitoring of intraocular pressure in glaucoma management: a retrospective review. *J. Glaucoma* **12**, 232–236 (2003).
14. Jiang, N., Montelongo, Y., Butt, H. & Yetisen, A. K. Microfluidic contact lenses. *Small* **14**, e1704363 (2018).
15. Kim, J. et al. Wearable smart sensor systems integrated on soft contact lenses for wireless ocular diagnostics. *Nat. Commun.* **8**, 14997 (2017).
16. Senior, M. Novartis signs up for Google smart lens. *Nat. Biotechnol.* **32**, 856 (2014).
17. Shin, H. et al. Recent progress on wearable point-of-care devices for ocular systems. *Lab Chip* **21**, 1269–1286 (2021).
18. Zhu, Y. et al. Lab-on-a-contact lens: recent advances and future opportunities in diagnostics and therapeutics. *Adv. Mater.* **34**, e2108389 (2022).
19. F. Han, F. et al. Smart contact Lenses: from rational design strategies to wearable health monitoring. *Chem. Eng. J.* **497** (2024).
20. Liu, X. et al. Smart contact lenses for healthcare monitoring and therapy. *ACS Nano* **18**, 6817–6844 (2024).
21. Yao, G. et al. Snowflake-inspired and blink-driven flexible piezoelectric contact lenses for effective corneal injury repair. *Nat. Commun.* **14**, 3604 (2023).
22. Yao, G., Li, P., Liu, M., Liao, F. & Lin, Y. Smart contact lenses: Catalysts for science fiction becoming reality. *Innov. (Camb.)* **5**, 100710 (2024).
23. Kim, J. et al. Intraocular pressure monitoring following islet transplantation to the anterior chamber of the eye. *Nano Lett.* **20**, 1517–1525 (2020).
24. Kim, J. et al. A soft and transparent contact lens for the wireless quantitative monitoring of intraocular pressure. *Nat. Biomed. Eng.* **5**, 772–782 (2021).
25. Kim, T. Y. et al. Wireless theranostic smart contact lens for monitoring and control of intraocular pressure in glaucoma. *Nat. Commun.* **13**, 6801 (2022).
26. Moreddu, R. et al. Stretchable nanostructures as optomechanical strain sensors for ophthalmic applications. *ACS Appl. Polym. Mater.* **3**, 5416–5424 (2021).
27. Yang, C. et al. Intelligent wireless theranostic contact lens for electrical sensing and regulation of intraocular pressure. *Nat. Commun.* **13**, 2556 (2022).
28. Ye, Y. et al. Smart contact lens with dual-sensing platform for monitoring intraocular pressure and matrix metalloproteinase-9. *Adv. Sci. (Weinh.)* **9**, e2104738 (2022).
29. Zhang, J. et al. Smart soft contact lenses for continuous 24-h monitoring of intraocular pressure in glaucoma care. *Nat. Commun.* **13**, 5518 (2022).
30. Zhu, H. et al. Hydrogel-based smart contact lens for highly sensitive wireless intraocular pressure monitoring. *ACS Sens* **7**, 3014–3022 (2022).
31. Robinson, D. A. A method of measuring eye movement using a scleral search coil in a magnetic field. *IEEE Trans. Biomed. Eng.* **10**, 137–145 (1963).
32. Whitmire, E. et al. EyeContact: scleral coil eye tracking for virtual reality. Proceedings of the 2016 ACM International Symposium on Wearable Computers. pp 184–191 (2016).
33. Houben, M. M., Goumans, J. & van der Steen, J. Recording three-dimensional eye movements: scleral search coils versus video oculography. *Invest. Ophthalmol. Vis. Sci.* **47**, 179–187 (2006).
34. Oyama, A. et al. Novel method for rapid assessment of cognitive impairment using high-performance eye-tracking technology. *Sci. Rep.* **9**, 12932 (2019).
35. Song, J. H., van de Groep, J., Kim, S. J. & Brongersma, M. L. Non-local metasurfaces for spectrally decoupled wavefront manipulation and eye tracking. *Nat. Nanotechnol.* **16**, 1224–1230 (2021).
36. Shi, Y. et al. Eye tracking and eye expression decoding based on transparent, flexible and ultra-persistent electrostatic interface. *Nat. Commun.* **14**, 3315 (2023).
37. Pu, X. et al. Eye motion triggered self-powered mechnosensational communication system using triboelectric nanogenerator. *Sci. Adv.* **3**, e1700694 (2017).
38. Skoglund, M. A. et al. Comparing In-ear EOG for eye-movement estimation with eye-tracking: accuracy, calibration, and speech comprehension. *Front. Neurosci.* **16**, 873201 (2022).
39. Zhu, H. et al. Frequency-encoded eye tracking smart contact lens for human-machine interaction. *Nat. Commun.* **15**, 3588 (2024).
40. Wang, S. et al. Flexible optoelectronic multimodal proximity/pressure/temperature sensors with low signal interference. *Adv. Mater.* **35** (2023).
41. Zhu, H., Luo, H., Cai, M. & Song, J. A multifunctional flexible tactile sensor based on resistive effect for simultaneous sensing of pressure and temperature. *Adv. Sci.* **11** (2023).
42. Yao, G. et al. A self-powered implantable and bioresorbable electrostimulation device for biofeedback bone fracture healing. *Proc Natl Acad Sci USA* **118** (2021).
43. Z. Qi, Z. et al. Reconfigurable flexible electronics driven by origami magnetic membranes. *Adv. Mater. Technol.* **6** (2021).
44. Miao, L. et al. 3D temporary-magnetized soft robotic structures for enhanced energy harvesting. *Adv. Mater.* **33**, e2102691 (2021).
45. Xie, M. et al. Multifunctional flexible contact lens for eye health monitoring using inorganic magnetic oxide nanosheets. *J. Nanobiotechnol.* **20**, 202 (2022).
46. Chen, G.-Z., Chan, I.-S. & Lam, D. C. C. Capacitive contact lens sensor for continuous non-invasive intraocular pressure monitoring. *Sens. Actuators, A* **203**, 112–118 (2013).
47. Jang, J. et al. Smart contact lens and transparent heat patch for remote monitoring and therapy of chronic ocular surface inflammation using mobiles. *Sci Adv* **7** (2021).
48. Oh, E. J. et al. Simulation analysis of flow rate variability during microinfusions: the effect of vertical displacement and multidrug infusion in conventional infusion pumps versus new cylinder-type infusion pumps. *Anesth. Analg.* **134**, 59–68 (2022).
49. Weiss, M., Wendel-Garcia, P. D., Cannizzaro, V., Buehler, P. K. & Kleine-Brueggeny, M. Effect of central venous pressure on fluid delivery during start-up of syringe infusion pumps for microinfusion. *Paediatr. Anaesth.* **33**, 837–843 (2023).
50. Freeman, D. K. & Byrnes, S. J. Optimal frequency for wireless power transmission into the body: efficiency versus received power. *IEEE Trans. Antennas Propag.* **67**, 4073–4083 (2019).